Mass-Producible 2D Nanocomposite-Based Temperature-Independent All-Printed Relative Humidity Sensor

Zarak Jamal Khattak, Memoon Sajid,* Mazhar Javed, Hafiz Muhammad Zeeshan Rizvi, and Faisal Saeed Awan

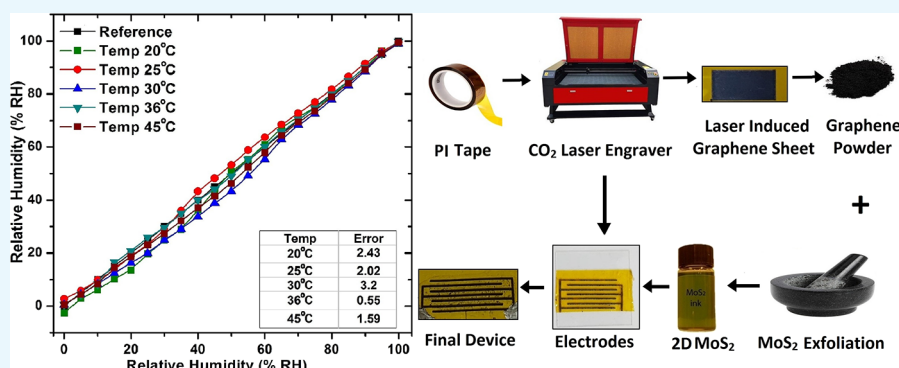Read Online

ACCESS | 📊 Metrics & More | 📖 Article Recommendations | 🆂🅸 Supporting Information

ABSTRACT: Relative humidity sensors are widely studied under the categories of both environmental and biosensors owing to their vast reaching applications. The research on humidity sensors is mainly divided into two concentration areas including novel material development and novel device structure. Another approach focuses on the development of printed sensors with performance comparable to the sensors fabricated via conventional techniques. The major challenges in the research on relative humidity sensors include the range of detection, sensitivity (especially at lower %RH), transient response time, and dependence on temperature. Temperature dependence is one of the least studied parameters in relative humidity sensor development. In this work, relative humidity sensors were fabricated using all-printed approaches that are also compatible with mass production, resulting in low cost and easy development. Laser-induced graphene (LIG)-based printed electrodes were used as the transducers, while the 2D MoS_2 and graphene nanocomposite was used as the active layer material with the built-in property of temperature independence. The exfoliation process of 2D MoS_2 was based on wet grinding, while graphene for the active layer was obtained by scratching the graphene grown on the polyimide (PI) surface via laser ablation. The resulting sensors showed an excellent output response for a full range of 0%RH to 100%RH, having no dependence on the surrounding temperature, and excellent response and recovery times of 4 and 2 s, respectively. The developed sensors can be confidently employed for a wide range of humidity sensing applications where the temperature of the surrounding environment is not constant.

1. INTRODUCTION

The presence of water in its gaseous state in air is referred to as humidity, and its understanding and measurement are significantly important. The need for fabricating state-of-the-art humidity sensors has recently escalated because humidity finds its applications in the monitoring of the environment[1] as well as various industries such as agriculture, health,[2] food industry,[3] medicine,[4] etc. Sensors have been fabricated using various materials such as 2D materials,[5−7] metallic oxides,[8−10] nanocrystals,[11] organic materials,[12] polymers,[13] paper-based sensitive materials,[14] and others[15−17] and by using a number of different fabrication techniques including sputtering,[18] thermal evaporation,[19] lithography,[20] printing,[21] spin coating,[22] spray deposition,[23] etc. Different types of structures have been used as transducers including interdigitated electrodes (IDTs),[24]

FETs,[25] chemiresistors,[26] optical fibers,[27] crystal oscillators,[28] capacitors,[29] etc. All of the research in this field focuses on developing low-cost and high-performing sensors using non-conventional, environmentally friendly, and facile fabrication techniques.

Various fabrication techniques are being developed for the fabrication of electronic devices including sensors,[30] transistors,[31] memory devices,[32] and other systems. Different types of
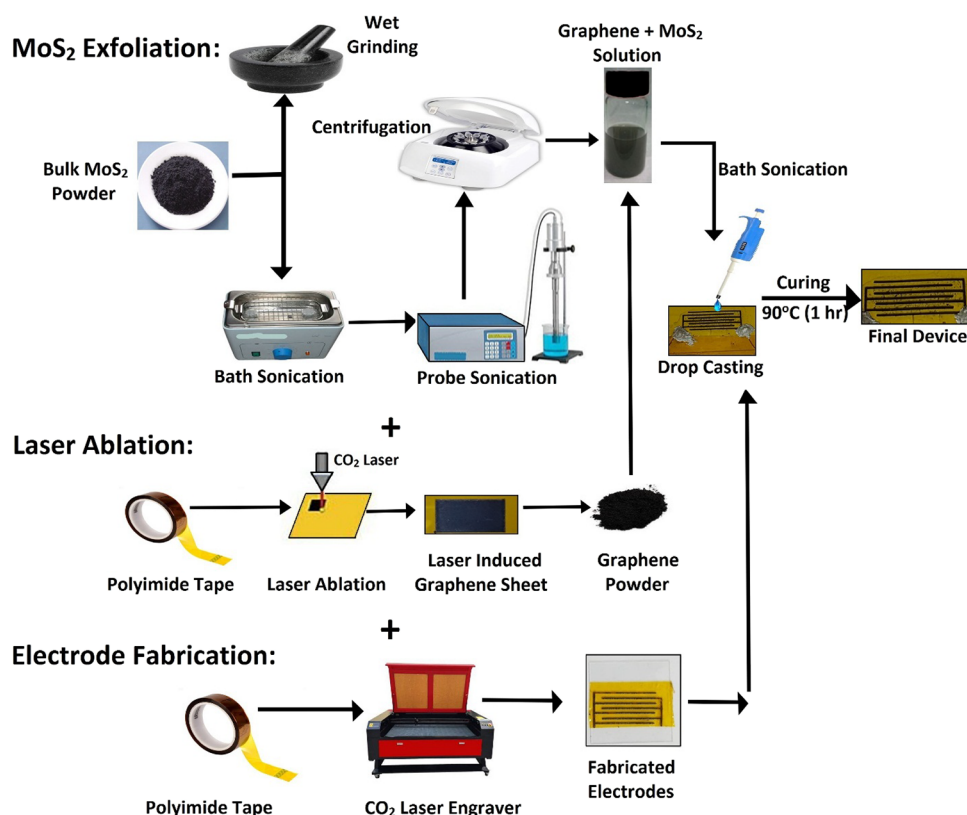
Figure 1. Step-by-step material synthesis and sensor fabrication process showing the exfoliation of bulk MoS_2 into 2D flakes, the growth of graphene through laser ablation, patterning of transducer electrodes, and the formation of the active layer and contacts for the final device.

materials are also being explored that are compatible with the available fabrication techniques for different types of devices. Printed electronics has revolutionized the prototyping by providing a simple, cost-effective, and quick solution for preliminary device testing and optimization as compared to the conventional device fabrication techniques. The major hurdle in using printed electronics to mass produce electronic devices like sensors is the unavailability of materials compatible with the process or the materials having lower performance when compared to their conventional counterparts for the same types of devices.[33] Printed humidity sensors have been fabricated using a variety of materials with a major portion consisting of polymers and composites, oxides, nanomaterials, 2D materials, etc.[34−38] The polymer-based materials are relatively easier to use in printing of devices, but the performance of polymer-based humidity sensors has limitations of a lower range of detection, usually a slower transient response, degradation, and significant dependence on the surrounding temperature.[39] Oxides on the other hand are extremely difficult to print, while nanocomposites also have similar problems as those of polymers.[40,41] Researchers have tried to address some of the issues while compromising on the others. In addition, the transducer electrodes in printed electronic devices are generally metallic materials that are very expensive and are difficult to be patterned without wastage.

2D materials, graphene, carbon nanotubes, and their composites with polymers[42−44] have been recently investigated for their ability to sense humidity in printed sensors. 2D materials have proven to be an excellent choice because of their ideal electrical and morphological properties and their ability to detect lower levels of humidity.[45] The hurdle with using 2D materials like MoS_2 nanoflakes, graphene, and others is their

difficulty in being mass-produced.[46] In addition, while 2D materials address most of the performance limitations associated with various categories of materials, temperature dependence still remains an issue in most cases.

Graphene, which belongs to the 2D family of materials, has been deemed to be an excellent candidate for humidity sensing owing to its properties like high electron mobility ($200,000 \ cm^2 \ (V_s)^{-1}$), high specific surface area ($2600 \ m^2 g^{-1}$), chemisorption of water molecules, and inertness toward various gases.[47−50] The porous structure of graphene makes it ideal for applications like composite fillers, energy-storing devices, biosensors, etc.[51,52] Traditional methods for the fabrication of graphene require either very high temperatures[53] or a step-wise chemical reaction,[54,55] which not only makes the entire process costly but also time-consuming and with low yield. Similarly, other 2D materials like MoS_2, hBN, $MoSe_2$, WSe_2, etc., also offer excellent sensing properties like graphene, but their fabrication methods have many limitations as of graphene.[56]

In 2014, Tour et al. fabricated graphene through laser ablation of the polyimide (PI) surface and termed it as laser-induced graphene (LIG). A CO_2 laser was used to grow graphene on the surface of PI tape under ambient conditions.[57] LIG was found to possess the same porous structure as that of normal graphene, and its electrical characteristics resembled those of high-quality reduced graphene oxide (rGO). The computer-controlled laser scribing system removes the constraint on the patterning of the electrodes and other graphene-based structures.[58,59] Furthermore, LIG has proved to be nontoxic, which supports its use in biological applications as well.[60] Ever since its discovery, vast research has been conducted on this subject,[45,61−63] concluding that through laser patterning, ideal properties of rGO can be achieved through a much cheaper and facile procedure.

Similarly, other 2D materials like MoS_2, hBN, etc., have also been exfoliated into 2D flakes using mass-producible methods like wet grinding,[64] acid-based intercalation, etc. Wet grinding is a simple and low-cost method, while intercalation is expensive and complicated.

This work focuses on combining the three focus areas of research in relative humidity sensors by developing an all-printed novel humidity sensor based on a 2D nanocomposite of graphene and MoS_2 that is inherently independent of the effect of temperature, requiring no post-data processing or signal conditioning without compromising the overall performance of the sensors. The transducer electrodes were also based on LIG patterns, while both the active layer and 2D materials were fabricated using mass production-compatible methods. The use of the composite results in the overall temperature-independent behavior of the sensor while retaining the ideal sensing properties of the 2D materials.

2. EXPERIMENTAL SECTION

2.1. Materials and Methods. Ultrafine powder of bulk MoS_2 with a purity of 99% was purchased from Graphene Supermarket. Twenty grams of pristine bulk MoS_2 was ground in a mortar by adding 1 mL of ethanol with a purity of 99.9%. The paste was continuously ground for one and half hour and was then left to dry at room temperature. Ten grams of the dried powder was then dispersed in 100 mL of ethanol and water-based solvent prepared in equal ratio. The solution was first bath-sonicated for 30 min to separate the agglomerated particles and was then probe-sonicated for 1 h to exfoliate the ground MoS_2 flakes into 2D few and monolayered sheets. Centrifugation was then performed at 4000 rpm for 30 min to separate the bulk from exfoliated 2D flakes. The resulting supernatant was extracted after centrifugation to separate the exfoliated 2D flakes from the unexfoliated bulk particles. The residue was dried and weighted to calculate the concentration of MoS_2 in the solution by subtracting it from the initial 10 g. The resulting solution was found to have ~3 g exfoliated 2D MoS_2 few and monolayered flakes in 60 mL solution or a concentration of 5 wt %/vol. The wet grinding-based exfoliation method is well suited for mass production of 2D MoS_2 flakes, especially for applications like sensors where few to monolayered sheets are acceptable for the job.[65] The step-by-step exfoliation process schematic is presented in Figure 1.

Graphene for the active layer was grown on the surface of polyimide (PI) tape (Kapton Tape) through the direct laser ablation process. A CO_2 laser mounted on a 2-axis CNC router (4040A 50 W Laser Engraver) was used as the source. The laser power was set at 5 W by adjusting the PWM at 10%, while the relative bed speed was set at 90 mm/s to make 2 cm × 2 cm rectangular sheet patterns on the PI surface. Under the influence of the CO_2 laser, the polyimide film reaches a temperature of more than 2400 K, resulting in the precursor pyrolysis. This leads to emission of volatile gases such as CO_2 and H_2 along with the conversion of the sp^3 carbon atoms to sp^2 carbon atoms. This causes the distinct morphology and the porous structure of graphene.[66] During this process, the cooling and heating of the PI film happen abruptly, resulting in the formation of five-, six-, and seven-membered rings of carbon.[67] The graphene powder was obtained by scratching off the LIG sheet of the PI surface using a sharp blade.

The 2D nanocomposite solution for the active layer of the sensor was prepared by adding 0.3 g of powdered graphene to 10 mL of the prepared MoS_2 solution, thus resulting in a final

suspension with 5 wt %/vol MoS_2 and 3 wt %/vol graphene. The suspension was again bath-sonicated for 30 min to remove any agglomeration of particles and homogenize the 2D nano-composite before final deposition as the active layer thin film. The resistance of MoS_2 increases with increasing temperature with a slope of ~0.07,[68] while the resistance of graphene decreases with increasing temperature with a slope of ~0.12,[69] showing the opposite behavior of both materials toward the change in temperature. The final ratio of MoS_2 vs graphene in the composite was selected to be ~1.67, which is equal to the inverse of the ratio of resistance temperature coefficients of both materials to cancel out the effect of temperature in the final composite.

2.2. Device Fabrication. Carbon-based interdigitated transducer (IDT) electrodes were fabricated on a PI substrate mounted on a glass slab through the laser ablation process as discussed above. The printing parameters were optimized to achieve patterns without any defects and with high conductivity. Optimized parameters for electrode patterning are presented in Table 1, while the fabrication process schematic is presented in

Table 1. Optimized Parameters for Fabrication of Transducer Electrodes for the Device Using Laser Ablation

parameter	optimized value
laser current (%)	10%
laser power (W)	5 W
stand-off distance (mm)	20 mm
relative stage speed (mm/s)	90 mm/s
electrode line width (mm)	0.45 mm
gap between adjacent electrodes (mm)	0.65 mm

Figure 1 along with the actual images of the fabricated devices. The 2D nanocomposite-based humidity sensing active layer was deposited by drop-casting 30 μL solution onto the fabricated electrodes using a micropipette. The initial devices were fabricated using a manual hand pipette, but later on, an automated micropipetting system was developed to complete an all-printing CNC-based automated fabrication system. The automated pipetting system is presented in Figure S1. Silver contacts were made to connect wires to the device for characterization, and the devices were then sintered at 90 °C for 1 h to cure the active layer by evaporating the solvent and to sinter the silver contacts.

2.3. Sensor Characterization. The physical, chemical, morphological, and electrical properties of the devices were investigated using various standard techniques to validate and evaluate their characteristics and performance. Optical micros-copy was used to determine the physical state of devices. Field emission scanning electronic microscopy (FESEM) was performed using a Carl Zeiss EVO 18 with integrated energy dispersive spectroscopy (EDS) to investigate the device morphology and elemental analysis. A LabRAM HR Raman spectrometer was used to investigate the chemical composition and energy states to determine the type of chemical structure present in the active layer. PHI Quantera II VG X-ray photoelectron spectroscopy (XPS) was used to ensure the presence of 2D MoS_2 flakes after exfoliation.

For the characterization of the sensor's output response, an in-house-developed automatically controlled environmental cham-ber was employed.[65] The temperature inside the chamber was controlled through an inductive heating element, and humidity was controlled using dry nitrogen gas and a desktop humidifier.
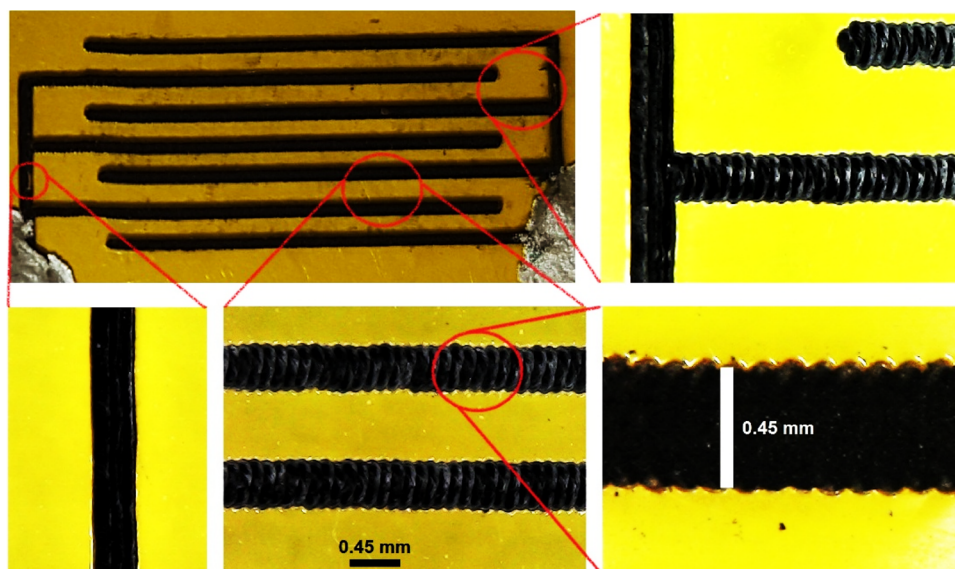
Figure 2. Optical microscopic images at different magnifications of the fabricated LIG patterns for transducer electrodes.
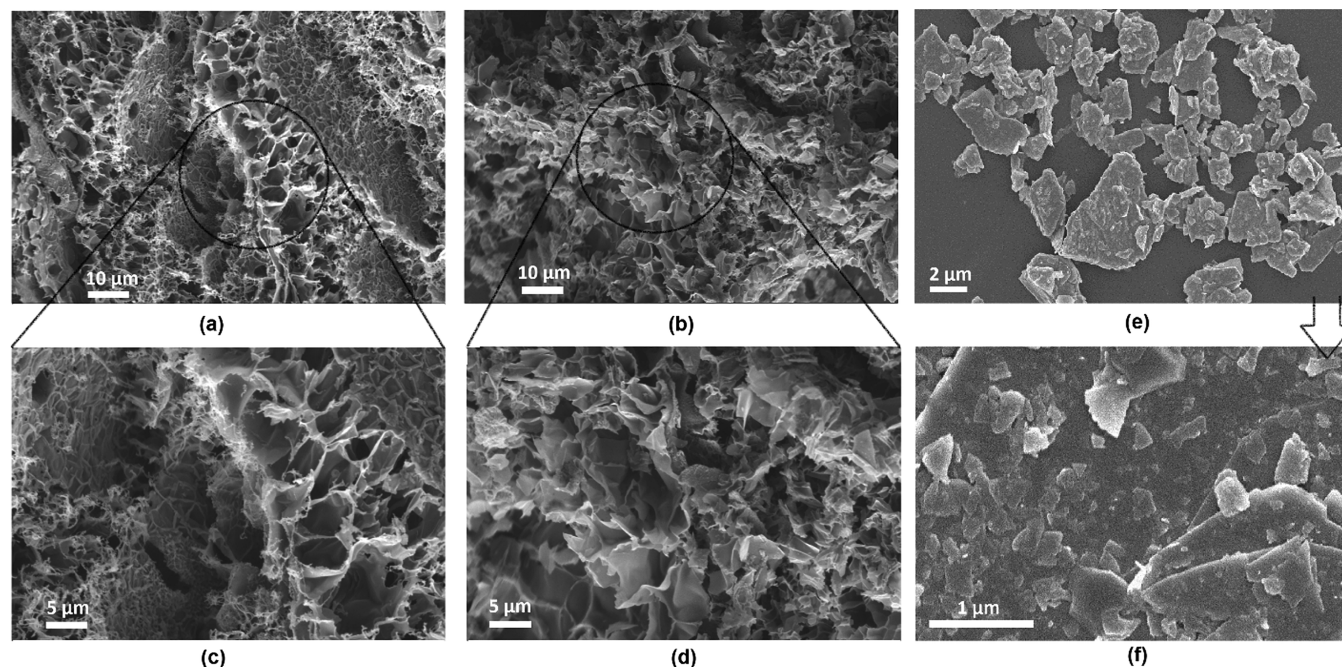

Figure 3. SEM images of the materials showing (a) LIG patterns on the PI surface (1 kX@5 kV), (b) graphene + MoS$_2$ active layer thin film (1 kX@5 kV), (c) zoomed view of LIG patterns (2 kX@5 kV), (d) zoomed view of the active layer thin film showing highly porous morphology (2 kX@5 kV), (e) bulk MoS$_2$ chunks (5 kX@5 kV), and (f) exfoliated 2D MoS$_2$ flakes (25 kX@5 kV).

The characterization setup schematic is presented in Figure S2. For reference temperature and humidity measurement, a precalibrated Bosch BME 280 sensor was used, while the electrical characteristics of the fabricated device in response to changing humidity and temperature were recorded using an Applent AT-825 digital LCR meter operating at 0.6 V$_{rms}$ and 1 kHz. All devices were time-synced through a customized software, and the data from both reference sensors and the device under testing was plotted in real time on a computer while simultaneously logging it for recording and later use. A cycling test of the sensors was performed by switching between one stream of air saturated with water vapor and one stream of dry nitrogen. The active area of the sensors was placed perpendicularly to the joint opening of the two streams. The

distance was kept at 2 cm. Valves controlling humid stream and dry nitrogen stream were opened and closed to switch between high and low humidity. The streams were switched after getting a stable/saturated curve of the sensor's output. The reference sensor recorded a high side humidity of ∼97%RH and a low side humidity of ∼4%RH.

3. RESULTS AND DISCUSSION

3.1. Morphological and Chemical Characterizations.
The materials used in fabrication of the devices were characterized for their physical morphology first to ensure the formation of physical 2D flakes in the case of MoS$_2$ and ascertain that the LIG patterns were not damaged and were neither under-
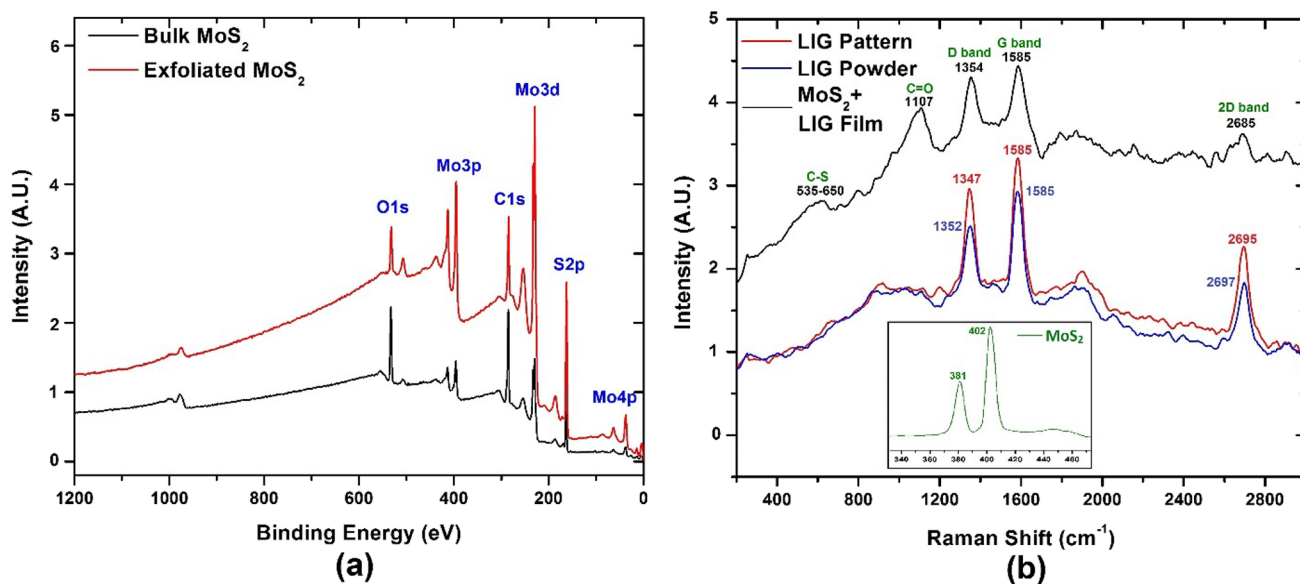
Figure 4. Chemical characterization of active layer materials showing (a) the XPS energy spectrum of MoS_2 and (b) RAMAN spectra of LIG and MoS_2 + LIG composite thin film.

nor overexposed. Optical microscopic images of the LIG patterns are presented in Figure 2 at various magnifications, confirming that the fabricated patterns were continuous and without any physical defects. The images of the IDT fingers show that the achieved electrode finger width was 0.45 mm, while the gap between two fingers was ∼0.6 mm.

The surface SEM images of LIG patterns fabricated for transducer electrodes presented in Figure 3a,c show the distinct porous structure of the graphene flake layer grown on the PI surface as expected. The SEM images of the graphene + MoS_2 active layer thin film presented in Figure 3b,d show that the scratched off graphene retained its specific porous structure without any degradation or defects. This porous morphology of the active layer is crucial for humidity and gas sensing applications where a higher surface area-to-volume ratio results in better adsorption and sensitivity. The surface SEM images of bulk and exfoliated MoS_2 presented in Figure 3e,f show that the bulky chunks were successfully exfoliated into 2D flakes through the wet grinding process as explained earlier.

Chemical and structural properties of the LIG and 2D MoS_2 flakes were investigated through Raman spectroscopy, X-ray photoelectron spectroscopy (XPS), and energy dispersive spectroscopy (EDS). The results of XPS for MoS_2 presented in Figure 4a show distinct peaks for Mo3p, Mo3d, Mo4p, and S2p, confirming the presence of MoS_2. The comparison of the spectra for exfoliated and bulk MoS_2 indicates a sharp rise in the intensity of Mo and S peaks for exfoliated flakes when compared to the bulk ones, while the carbon and oxygen peaks remain the same, which is due to the carbon-based tape used in this characterization for sample holding. Raman spectroscopy results presented in Figure 4b compare the spectra for LIG patterns directly grown onto the PI surface, the powder obtained by scratching the grown LIG layer, and the thin film based on the 2D nanocomposite of LIG and MoS_2 flakes. The spectra for pure LIG show distinct peaks at 1350, 1585, and 2695 cm^{-1} corresponding to the signature D-band, G-band, and 2D-band of graphene, respectively.[70] The D-band is associated with the higher energy sp^3 defect sites, while the G-band is associated with the lower energy sp^2 carbon bonds.[70] The intensity of the

G-band is higher in all cases, indicating a higher number of low-energy binding sites for chemisorption of water atoms. The 2D peak can be fitted with just only a Lorentzian peak centered at around 2700 cm^{-1}, which is the same as that of single-layered graphene, but the larger width indicates that the structure is similar to 2D graphite, which consists of randomly stacked graphene single layers along the c-axis.[57] The intensity of both the D- and G-bands is lower in the composite when compared to pure graphene, indicating a decrease in the surface area of graphene after interaction with MoS_2. Furthermore, a broad peak at 1107 cm^{-1} in the composite spectrum represents C=O, which indicates the formation of oxides of graphene at the defect sites during the process of making the solution for the nanocomposite and annealing of the thin film.[71] A wide envelope in the range of 535 to 650 cm^{-1} indicates the formation of some C−S bonds, confirming the physical interaction of graphene and 2D MoS_2 flakes. The intensity and sharpness of the C−S peak are however very low, indicating the weaker interaction of MoS_2 and graphene at various locations spread throughout the thin film rather than formation of a widespread network of 2D heterojunctions. This will enable direct electron transfer between graphene and MoS_2 but will not result in formation of a visible barrier throughout the material. The signature peaks of MoS_2 at 402 and 381 cm^{-1} are not visible in the Raman spectrum of the composite due to their relatively low intensities, but a separate Raman spectrum of exfoliated MoS_2 flakes presented as the inset in Figure 4b indicates the two peaks, clearly confirming the formation of 2D flakes. Energy dispersive spectroscopy (EDS) was also performed to confirm the presence of both carbon and MoS_2 in the active layer, and the results presented in Figure S3 ascertain the presence of all the elements.

3.2. Electrical Response and Behavior. The fabricated humidity sensing devices consisted of IDT-type electrode pairs with an active layer of the 2D MoS_2 and graphene composite deposited on the sensing area. The sensors respond to the change in surrounding environment humidity in terms of the change in their impedance. The percent relative humidity of a controlled environment was varied from 0%RH to 100%RH,
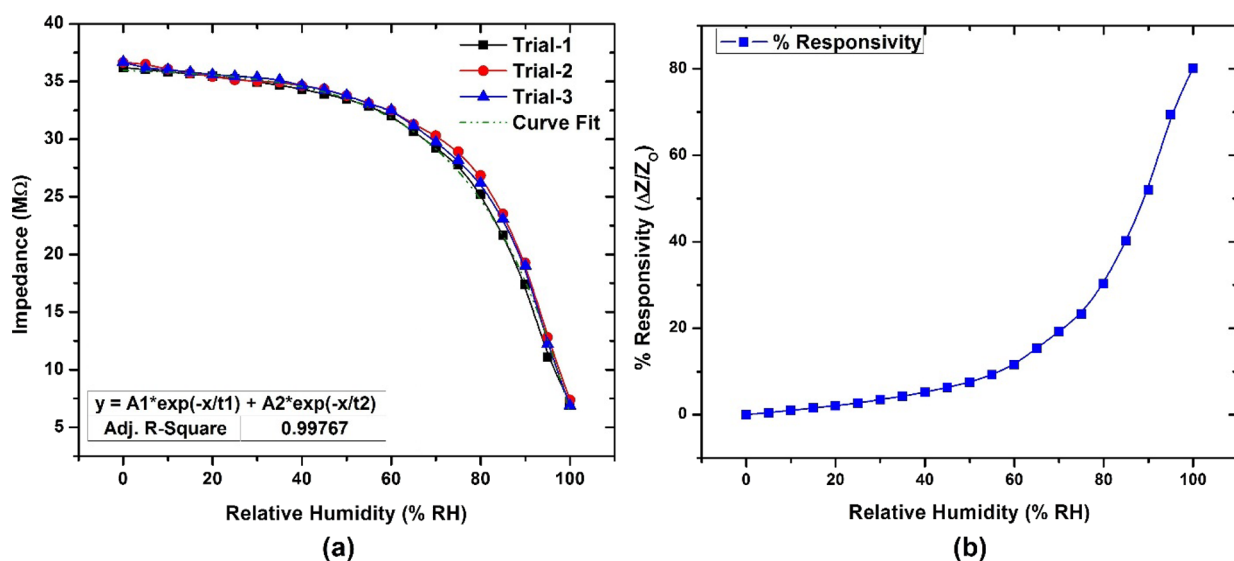
Figure 5. Response of humidity sensors showing (a) impedance vs %RH for three independent trials at 30 °C and (b) responsivity curve of the sensors showing the percent change in response at different relative humidity levels.
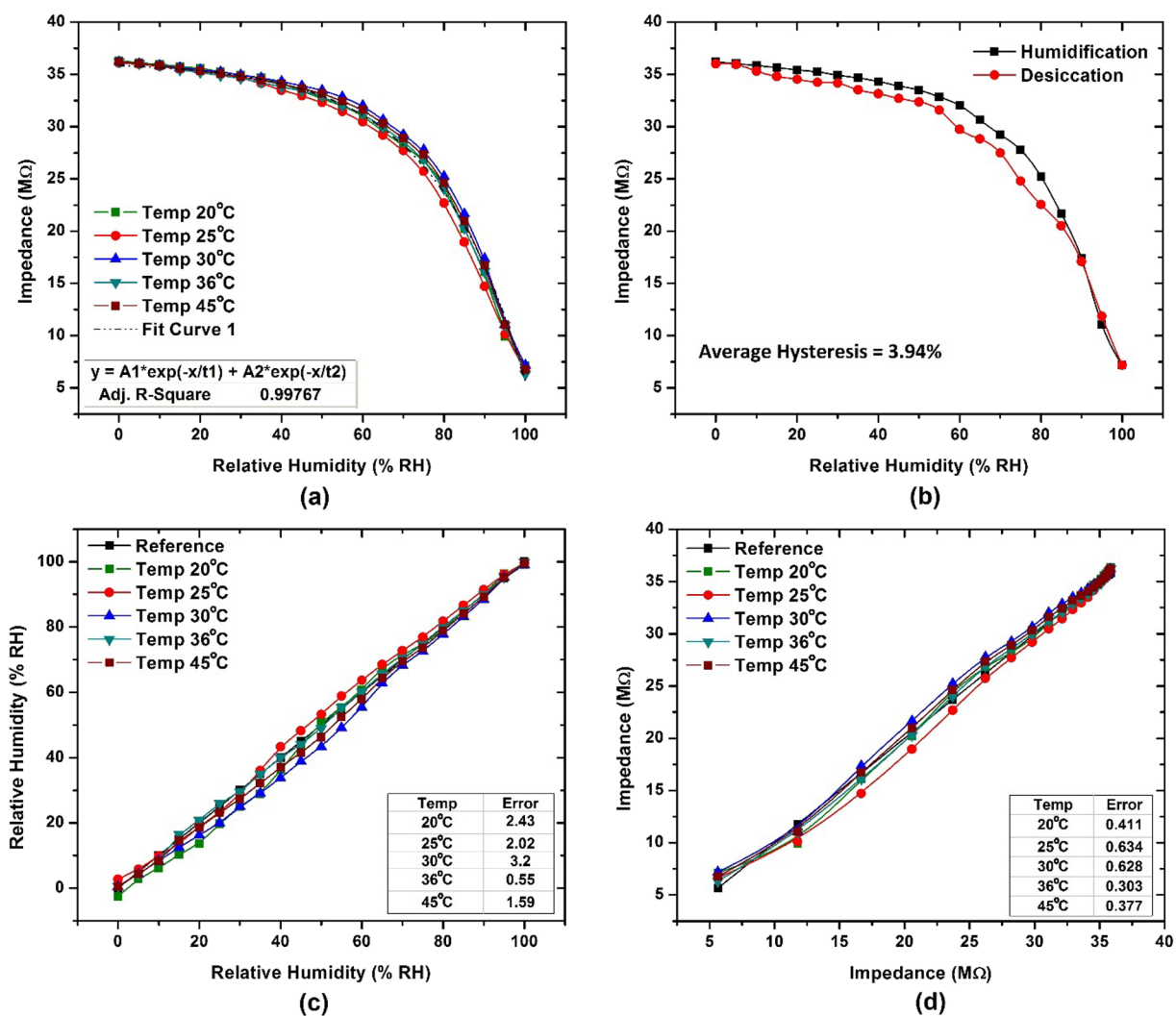

Figure 6. Response of devices toward the change in temperature: (a) impedance curves at different temperatures, (b) hysteresis curve for humidification and desiccation, (c) errors in relative humidity at various temperatures, and (d) errors in impedance at various temperatures.
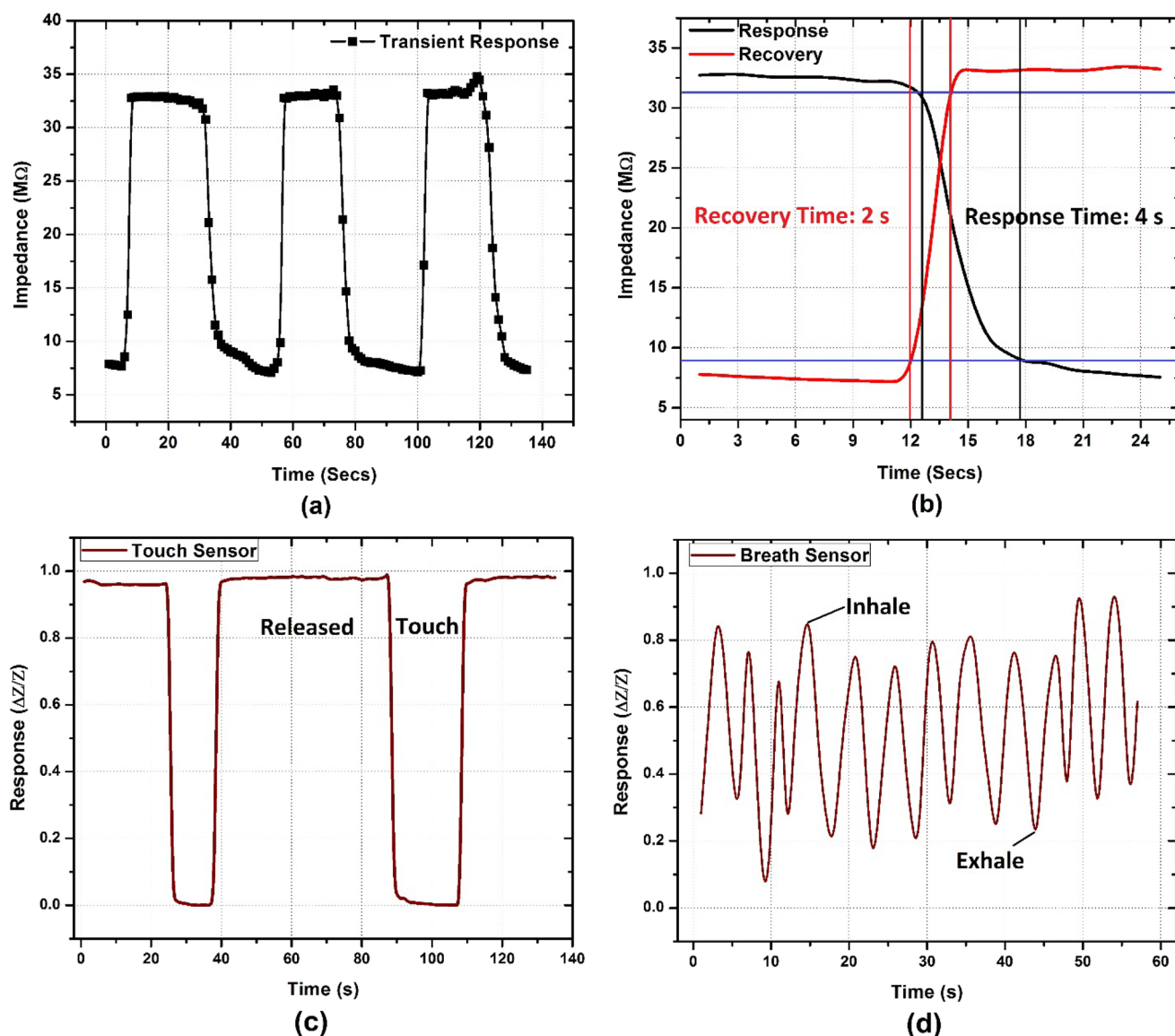
Figure 7. Performance of the fabricated sensors showing (a) the transient response curve, (b) response and recovery times, (c) touch sensing, and (d) breath detection.

and enough time was provided to the output of fabricated devices to get stable. Impedance readings of the fabricated sensors were recorded at intervals of 5%RH for three independent trials at three various times. The results presenting the relationship of the impedance output of the fabricated sensor versus the changing relative humidity of the environment are presented in Figure 5. The temperature for all three trials was kept constant at 30 °C inside the controlled environment test chamber.

Results presented in Figure 5a show that the impedance of sensors based on the 2D nanocomposite decreases exponentially with increasing relative humidity of the surrounding environment. It can be further observed that the sensors show a stable response toward the full range of relative humidity from 0%RH to 100%RH without any saturation. Figure 5b shows that the sensitivity or responsivity of the sensors for the lower half of relative humidity (0%RH to 50%RH) is also quite reasonable at ∼8% (50 kΩ/%RH), after which it increases exponentially up to ∼80% (385 kΩ/%RH). It was also calculated from the results that the absolute average error for the three trials was just 1.9%,

indicating the excellent reproducibility of the fabricated sensors under given conditions. The mechanism behind humidity sensing for pure MoS_2 and pure graphene has been investigated individually in previous research works. MoS_2 responds to the change in humidity through absorption of water molecules at the defect sites of the hexagonal 2D structure and the terminal ends of the flakes.[21] Mechanical wet grinding results in formation of a relatively larger number of defect sites as compared to MoS_2 synthesis using hydrothermal and chemical exfoliation methods, making wet grinding the ideal process for humidity sensing applications.[65] MoS_2 responds to low relative humidity levels, but the response quickly saturates near 40%RH, thus reducing the range of detection.[21] Graphene-based humidity sensors on the other hand respond to the change in relative humidity through both adsorption and absorption. The sensitivity of pure graphene-based sensors toward lower humidity levels is very low, and the overall change in resistance is very small.[72] In addition, the resistance of graphene-based humidity sensors is also highly dependent on changes in surrounding temperature because the resistance of pure graphene decreases with

Table 2. Comparison of Performance and Fabrication Methods of the Current Sensor with the Literature and Commercially Available Relative Humidity Sensors

materials	fabrication method	sensing mechanism	%RH range	sensitivity	response/ recovery time	% error	temperature compensated	reference
amorphous PEO	reverse offset printing	impedance	0−75%	100 mV/%RH	2.9/1.9 s	1.24%	YES (conditioning circuit)	78
2D MoS$_2$ + PEO	EHD printing	resistive	0−80%	85 kΩ/%RH	0.6/0.3 s	5.4%	YES (numerical with temp. sensor)	65
PEDOT:PSS-methyl red-graphene series	inkjet printing	impedance	0−100%	100 kΩ/%RH	1/3.5 s	2.2%	NO	22
TiSi$_2$	screen printing	capacitive	0−100%	63 kΩ/%RH	3 s/4 s	insignificant	NO	79
GO/PVA	heat & pull	optical fiber	20−100%	0.5290%/RH	147/293 s	3.11%	NO	80
porous LIGO	laser ablation printing	capacitive	11−97%	9150 pF/%RH	2 s	3.3%	NO	45
OR coating	fiber optic Braggs grating	Bragg's wavelength shift	11.3−97.3%	2.40 pm/%RH	655/370 s	4.16%	YES (uncoated reference subtraction)	81
PI coating	fiber optic Braggs grating	Bragg's wavelength shift	11−83%	1.5 pm/%RH			YES (numerical with temp. sensor)	82
HPP801A031	polymeric MEMS lithography	capacitive	1−99%	310 nF/%RH	3 s		NO	commercial
HTU31	MEMS lithography	resistive	0−100%	0.01 %RH resolution	5/10 s	2%	YES (numerical with temp. sensor)	commercial
HTU21D	MEMS lithography	resistive	0−100%	0.04 %RH resolution	5/10 s	5%	YES (numerical with temp. sensor)	commercial
Si7021	MEMS lithography	resistive	0−80%	0.7 %RH resolution	5/18 s	3%	YES (Undisclosed)	commercial
2D MoS$_2$ + graphene	laser ablation	impedance	0−100%	8% (0−50%RH), 80% (50−100% RH)	4/2 s	3.8%	YES (material-based self-compensation)	this work

increasing temperature, which is highly undesirable.[73] As the results presented in Figure 5 indicate, the 2D nanocomposite of MoS$_2$ and graphene addresses both the issues associated with the range of detection and sensitivity at lower humidity levels. The exfoliated 2D MoS$_2$ and graphene interact through carbon−sulfur (C−S) bonding between the layers[71] as eminent from the Raman results presented in Figure 4. The 2D sheets of graphene and MoS$_2$ bind together at various sites, allowing direct electron transfer between the two layers. Water molecules at lower percentage RH result in ionic plus proton hopping current in MoS$_2$,[74] while the hydroxyl ions bind to the lower-energy binding sites (sp^2) of graphene and to the free defect and edge sites of MoS$_2$, increasing its mobility due to the electron donor behavior of the hydroxyl ion and the n-type semiconducting properties of MoS$_2$.[75,76] At higher humidity levels, the resistance of the overall composite decreases due to adsorption and absorption of water molecules into the highly porous 2D nanocomposite. Furthermore, the temperature dependence and hysteresis of the composite-based sensor were also investigated by recording the full-range response curves at five different temperatures as presented in Figure 6.

The full response curves presented in Figure 6a show the excellent stability of the sensors toward changing surrounding temperature. One exponential equation for the impedance curve fit was derived for the response toward relative humidity at a single temperature as presented in Figure 6a. The same equation was then employed to calculate the humidity and impedance at different temperatures. Further details of the equation parameters are presented in Table S1. The comparison of calculated humidity levels with the reference shows absolute errors of 2.43, 2.02, 3.2, 0.55, and 1.59 for 20, 25, 30, 36, and 45 °C, respectively, as shown in Figure 6c, while the impedance curves obtained at 20, 25, 30, 36, and 45 °C have absolute errors of 0.411, 0.634, 0.628, 0.303, and 0.377, respectively, as shown in Figure 6d. The average percentage error for humidity was

calculated to be around 3.9% for 25 °C ΔT or 0.16%/°C. It can be noted that the reference sensor also has a maximum error of up to 3% in the measurement of relative humidity. Given the data, the sensors show almost independent behavior toward changing temperature and their output impedance is only effected by the change in relative humidity as desired. The temperature-independent behavior of the sensor is partially due to the chemical interaction of MoS$_2$ and graphene through the C−S bonds and mostly due to the fact that the mobility of MoS$_2$ decreases with increasing temperature,[77] while the conductivity of graphene increases with increasing temperature.[73] The opposite effect of the two is effectively canceled out in the composite-based sensor, resulting in the temperature-independent behavior of the device. This results in the high specificity and stability of the sensors, making them ideal for humidity measurement in environments where temperature is not constant. The hysteresis behavior of the sensor is presented in Figure 6b for the full cycle humidification and desiccation, showing an average hysteresis of 3.94% for the whole curve calculated using eq 1. The results show no permanent zero error and the output returning to the initial value eventually.

$$\text{average hysteresis} = \left[\sum_{k=0}^{n} \left| \frac{y_{k+1} - y_k}{y_{max} - y_{min}} \right| \right] / n \tag{1}$$

Other performance characteristics of the fabricated sensor like response and recovery times and the performance while being employed as a touch sensor and a breath detection sensor were investigated, and the results are presented in Figure 7.

Figure 7a shows the transient response curve of the fabricated sensor with excellent stability and reproducibility and no visible saturation or offset observed between cycles, indicating the low hysteresis of the device. The expanded curves presented in Figure 7b were used to calculate the response time and recovery

time of the sensor to get a stable response for 10% minimum and 90% maximum values of output. The sensors showed excellent response and recovery times of 4 and 2 s, respectively, which are comparable to the sophisticated sensors commercially available over the shelf. The behavior of sensors toward physical touch was also investigated with the results of Figure 7c showing very high sensitivity of the sensors toward touch and an excellent recovery back to the intrinsic value. The curves also show that there is no degradation or slope visible in the sensor's output before and after the touch. Finally, the breath detection results presented in Figure 7d indicate that the sensors can be used to detect normal breathing patterns with good reliability and low noise. The performance parameters and fabrication methods of the sensor were compared to those in the recent literature and the commercial sensors available in the market. The comparison presented in Table 2 clearly shows that the fabricated devices can be an excellent choice for low-cost, mass-produced, temperature-independent humidity sensors fabricated through laser patterning techniques.

4. CONCLUSIONS

Relative humidity sensors were successfully fabricated through laser patterning techniques compatible with mass production and automated manufacturing. Laser-induced graphene patterns grown on the polyimide surface were used as transducer electrodes, while the active sensing layer was based on the 2D nanocomposite of exfoliated MoS_2 flakes and graphene. The printing resolution of electrode patterns was mainly dependent on the laser power, relative speed of the stage and head, and the unit step mechanical resolution of stage movement. High-resolution microstepping CNC routers can be used to improve the resolution of electrode patterns. The material synthesis process to achieve the 2D nanocomposite for the active layer involved exfoliation of bulk MoS_2 powder through mechanical wet grinding, while 2D graphene was extracted from the grown LIG sheets. The sensors showed excellent sensitivity toward the full range of relative humidity (0%RH to 100%RH) with fast response and recovery times of 4 and 2 s, respectively. The fabricated sensors were inherently temperature-independent with their output impedance changing only in response to the change in humidity, making them highly specific and ideal for humidity-measuring applications where temperature is not constant. The sensors were also employed for breath detection and touch sensing, and the results showed a stable response. The developed methods and materials can be a step forward toward the development of high-performance sensing devices fabricated through automated printing compatible with scalable production.

ASSOCIATED CONTENT

Supporting Information

The Supporting Information is available free of charge at https://pubs.acs.org/doi/10.1021/acsomega.2c00850.

    Automated pipetting system, curve fitting equation and parameters, characterization setup details, and EDS spectra (PDF)

AUTHOR INFORMATION

Corresponding Author

Memoon Sajid − *Faculty of Electrical Engineering, Ghulam Ishaq Khan Institute of Engineering Sciences and Technology, Topi, K.P. 23640, Pakistan;* ● orcid.org/0000-0001-8820-0135; Phone: +923468710421; Email: memoonsajid@gmail.com

Authors

Zarak Jamal Khattak − *Faculty of Electrical Engineering, Ghulam Ishaq Khan Institute of Engineering Sciences and Technology, Topi, K.P. 23640, Pakistan*

Mazhar Javed − *Faculty of Electrical Engineering, Ghulam Ishaq Khan Institute of Engineering Sciences and Technology, Topi, K.P. 23640, Pakistan*

Hafiz Muhammad Zeeshan Rizvi − *Faculty of Electrical Engineering, Ghulam Ishaq Khan Institute of Engineering Sciences and Technology, Topi, K.P. 23640, Pakistan*

Faisal Saeed Awan − *Faculty of Electrical Engineering, Ghulam Ishaq Khan Institute of Engineering Sciences and Technology, Topi, K.P. 23640, Pakistan*

Complete contact information is available at:
https://pubs.acs.org/10.1021/acsomega.2c00850

Notes

The authors declare no competing financial interest.

REFERENCES

(1) Tai, H.; Wang, S.; Duan, Z.; Jiang, Y. Evolution of Breath Analysis Based on Humidity and Gas Sensors: Potential and Challenges. *Sens. Actuators, B* **2020**, *318*, No. 128104.

(2) Ma, L.; Wu, R.; Patil, A.; Zhu, S.; Meng, Z.; Meng, H.; Hou, C.; Zhang, Y.; Liu, Q.; Yu, R.; Wang, J.; Lin, N.; Liu, X. Y. Full-Textile Wireless Flexible Humidity Sensor for Human Physiological Monitoring. *Adv. Funct. Mater.* **2019**, *29*, 1−9.

(3) Yuhua, M.; Shuangyu, M.; Tieliu, W.; Weiling, F. Air-Flow Sensor and Humidity Sensor Application to Neonatal Infant Respiration Monitoring. *Sens. Actuators A* **1995**, *49*, 47−50.

(4) Chen, Z.; Lu, C. Humidity Sensors: A Review of Materials and Mechanisms. *Sens. Lett.* **2005**, *3*, 274−295.

(5) Zhen, Z.; Li, Z.; Zhao, X.; Zhong, Y.; Zhang, L.; Chen, Q.; Yang, T.; Zhu, H. Formation of Uniform Water Microdroplets on Wrinkled Graphene for Ultrafast Humidity Sensing. *Small* **2018**, *14*, No. e1703848.

(6) Choi, S. J.; Yu, H.; Jang, J. S.; Kim, M. H.; Kim, S. J.; Jeong, H. S.; Kim, I. D. Nitrogen-Doped Single Graphene Fiber with Platinum Water Dissociation Catalyst for Wearable Humidity Sensor. *Small* **2018**, *14*, No. e1703934.

(7) Guo, H.; Lan, C.; Zhou, Z.; Sun, P.; Wei, D.; Li, C. Transparent, Flexible, and Stretchable WS2 Based Humidity Sensors for Electronic Skin. *Nanoscale* **2017**, *9*, 6246−6253.

(8) Steele, J. J.; Taschuk, M. T.; Brett, M. J. Nanostructured Metal Oxide Thin Films for Humidity Sensors. *IEEE Sens. J.* **2008**, *8*, 1422−1429.

(9) Kupsta, M. R.; Taschuk, M. T.; Brett, M. J.; Sit, J. C. Reactive Ion Etching of Columnar Nanostructured TiO_2 Thin Films for Modified Relative Humidity Sensor Response Time. *IEEE Sens. J.* **2009**, *9*, 1979−1986.

(10) Shen, D.; Xiao, M.; Zou, G.; Liu, L.; Duley, W. W.; Zhou, Y. N. Self-Powered Wearable Electronics Based on Moisture Enabled Electricity Generation. *Adv. Mater.* **2018**, *30*, No. e1705925.

(11) Kano, S.; Kim, K.; Fujii, M. Fast-Response and Flexible Nanocrystal-Based Humidity Sensor for Monitoring Human Respiration and Water Evaporation on Skin. *ACS Sens.* **2017**, *2*, 828−833.

(12) Zhou, J.; Xiao, X.; Cheng, X. F.; Gao, B. J.; He, J. H.; Xu, Q. F.; Li, H.; Li, N. J.; Chen, D. Y.; Lu, J. M. Surface Modification of Polysquaraines to Sense Humidity within a Second for Breath Monitoring. *Sens. Actuators, B* **2018**, *271*, 137−146.

(13) Nohria, R.; Khillan, R. K.; Su, Y.; Dikshit, R.; Lvov, Y.; Varahramyan, K. Humidity Sensor Based on Ultrathin Polyaniline Film Deposited Using Layer-by-Layer Nano-Assembly. *Sens. Actuators, B* **2006**, *114*, 218−222.

(14) Dai, J.; Zhao, H.; Lin, X.; Liu, S.; Fei, T.; Zhang, T. Design Strategy for Ultrafast-Response Humidity Sensors Based on Gel Polymer Electrolytes and Application for Detecting Respiration. *Sens. Actuators, B* **2020**, *304*, No. 127270.

(15) Hajian, S.; Zhang, X.; Khakbaz, P.; Tabatabaei, S. M.; Maddipatla, D.; Narakathu, B. B.; Blair, R. G.; Atashbar, M. Z. Development of a Fluorinated Graphene-Based Resistive Humidity Sensor. *IEEE Sens. J.* **2020**, *20*, 7517−7524.

(16) Wang, S.; Chen, Z.; Umar, A.; Wang, Y.; Tian, T.; Shang, Y.; Fan, Y.; Qi, Q.; Xu, D. Supramolecularly Modified Graphene for Ultrafast Responsive and Highly Stable Humidity Sensor. *J. Phys. Chem. C* **2015**, *119*, 28640−28647.

(17) Neumeier, S.; Echterhof, T.; Bölling, R.; Pfeifer, H.; Simon, U. Zeolite Based Trace Humidity Sensor for High Temperature Applications in Hydrogen Atmosphere. *Sens. Actuators, B* **2008**, *134*, 171−174.

(18) Kunchakara, S.; Ratan, A.; Dutt, M.; Shah, J.; Kotnala, R. K.; Singh, V. Impedimetric Humidity Sensing Studies of Ag Doped MCM-41 Mesoporous Silica Coated on Silver Sputtered Interdigitated Electrodes. *J. Phys. Chem. Solids* **2020**, *145*, No. 109531.

(19) Yao, Y.; Huang, X. H.; Zhang, B. Y.; Zhang, Z.; Hou, D.; Zhou, Z. K. Facile Fabrication of High Sensitivity Cellulose Nanocrystals Based QCM Humidity Sensors with Asymmetric Electrode Structure. *Sens. Actuators, B* **2020**, *302*, No. 127192.

(20) Ko, J.; Yoon, Y.; Lee, J. Quartz Tuning Forks with Hydrogel Patterned by Dynamic Mask Lithography for Humidity Sensing. *Sens. Actuators, B* **2018**, *273*, 821−825.

(21) Siddiqui, G. U.; Sajid, M.; Ali, J.; Kim, S. W.; Doh, Y. H.; Choi, K. H. Wide Range Highly Sensitive Relative Humidity Sensor Based on Series Combination of MoS2 and PEDOT:PSS Sensors Array. *Sens. Actuators, B* **2018**, *266*, 354−363.

(22) Hassan, G.; Sajid, M.; Choi, C. Highly Sensitive and Full Range Detectable Humidity Sensor Using PEDOT:PSS, Methyl Red and Graphene Oxide Materials. *Sci. Rep.* **2019**, *9*, 15227.

(23) Songkeaw, P.; Onlaor, K.; Thiwawong, T.; Tunhoo, B. Transparent and Flexible Humidity Sensor Based on Graphene Oxide Thin Films Prepared by Electrostatic Spray Deposition Technique. *J. Mater. Sci.: Mater. Electron.* **2020**, *31*, 12206−12215.

(24) Wang, F.; Jian, J.; Geng, X.; Gou, G.; Cui, W.; Cui, J.; Qiao, Y.; Fu, J.; Yang, Y.; Ren, T. L. A Miniaturized Integrated SAW Sensing System for Relative Humidity Based on Graphene Oxide Film. *IEEE Sens. J.* **2020**, *20*, 9733−9739.

(25) Karimov, K. S.; Ahmed, M. M.; Saleem, M.; Shafique, S.; Akmal, M. Orange Dye Based Field Effect Transistor as Humidity Sensor. *Optoelectron. Adv. Mater., Rapid Commun.* **2020**, *14*, 416−420.

(26) Gupta, A.; Sakhuja, N.; Jha, R.; Bhat, N. Giant Humidity Responsiveness of Platinum Functionalized WS2Nanosheet Based Chemiresistors. In *Proceedings of IEEE Sensors*; 2020; Vol. *2020* Octob, DOI: 10.1109/SENSORS47125.2020.9278608.

(27) Owji, E.; Mokhtari, H.; Ostovari, F.; Darazereshki, B.; Shakiba, N. 2D Materials Coated on Etched Optical Fibers as Humidity Sensor. *Sci. Rep.* **2021**, *11* (), DOI: 10.1038/s41598-020-79563-w.

(28) Yu, X.; Chen, X.; Yu, X.; Chen, X.; Ding, X. A Quartz Crystal Microbalance (QCM) Humidity Sensor Based on a Pencil-Drawn Method with High Quality Factor. *IEEE Trans. Electron Devices* **2021**, *68*, 5149−5154.

(29) Kumar, A.; Wang, C.; Meng, F. Y.; Liang, J. G.; Xie, B. F.; Zhou, Z. L.; Zhao, M.; Kim, N. Y. Aerosol Deposited BaTiO3 Film Based Interdigital Capacitor and Squared Spiral Capacitor for Humidity Sensing Application. *Ceram. Int.* **2021**, *47*, 510−520.

(30) Kumar, P.; Khadtare, S.; Park, J.; Yadav, B. C. Fabrication of Leaf Shaped SnO2 Nanoparticles via Sol−gel Route and Its Application for the Optoelectronic Humidity Sensor. *Mater. Lett.* **2020**, *278*, 128451.

(31) Zhao, C.; Tan, C.; Lien, D. H.; Song, X.; Amani, M.; Hettick, M.; Nyein, H. Y. Y.; Yuan, Z.; Li, L.; Scott, M. C.; Javey, A. Evaporated Tellurium Thin Films for P-Type Field-Effect Transistors and Circuits. *Nat. Nanotechnol.* **2020**, *15*, 53−58.

(32) Jung, J.; Bae, D.; Kim, S.; Kim, H. D. Reduced Operation Current of Oxygen-Doped ZrN Based Resistive Switching Memory Devices

Fabricated by the Radio Frequency Sputtering Method. *Coatings* **2021**, *11*, 1−6.

(33) Rachim, V. P.; Park, S. M. Review of 3D-Printing Technologies for Wearable and Implantable Bio-Integrated Sensors. *Essays Biochem.* **2021**, 491−502.

(34) Choi, J.; Chen, Y.; Abbel, R.; Visagie, I.; Parker, K. Flexible Humidity Sensors for Wireless Monitoring Based on Electrospun Sulfonated Polyether Ether Ketone (SPEEK) Nanofibres. *Sens. Actuators, B* **2020**, *324*, 1−6.

(35) Choi, K. H.; Sajid, M.; Aziz, S.; Yang, B.-S. Wide Range High Speed Relative Humidity Sensor Based on PEDOT:PSS−PVA Composite on an IDT Printed on Piezoelectric Substrate. *Sens. Actuators A, Phys.* **2015**, *228*, 40−49.

(36) McGhee, J. R.; Sagu, J. S.; Southee, D. J.; Evans, P. S. A.; Upul Wijayantha, K. G. Printed, Fully Metal Oxide, Capacitive Humidity Sensors Using Conductive Indium Tin Oxide Inks. *ACS Appl. Electron. Mater.* **2020**, *2*, 3593−3600.

(37) Nadeem, I.; Memoon, S.; Khalid, R.; Tahseen, A. Q.; Shakeel, M.; Salman, A.; Mohsin, A. Fabrication of Temperature- and Humidity-Independent Silver Nanoparticle's Carbon Composite-Based Strain Sensor Through Additive Manufacturing Process. *3D Print. Addit. Manuf.* **2021**, DOI: 10.1089/3dp.2021.0032.

(38) Sajid, M.; Osman, A.; Siddiqui, G. U.; Kim, H. B.; Kim, S. W.; Ko, J. B.; Lim, Y. K.; Choi, K. H. All-Printed Highly Sensitive 2D MoS2 Based Multi-Reagent Immunosensor for Smartphone Based Point-of-Care Diagnosis. *Sci. Rep.* **2017**, *7*, 5802.

(39) Kim, S. W.; Rehman, M. M.; Sajid, M.; Rehman, M. M. U.; Gul, J.; Jo, J. D.; Choi, K. H. Encapsulation of Polyvinyl Alcohol Based Flexible Temperature Sensor through Spatial Atmospheric Atomic Layer Deposition System to Enhance Its Lifetime. *Thin Solid Films* **2019**, *673*, 44.

(40) Furqan, C. M.; Khan, M. U.; Awais, M.; Jiang, F.; Bae, J.; Hassan, A.; Kwok, H. S. Humidity Sensor Based on Gallium Nitride for Real Time Monitoring Applications. *Sci. Rep.* **2021**, *11*, 11088.

(41) Han, T.; Nag, A.; Afsarimanesh, N.; Mukhopadhyay, S. C.; Kundu, S.; Xu, Y. Laser-Assisted Printed Flexible Sensors: A Review. *Sensors* **2019**, *19*, 1−28.

(42) Zhao, Q.; Yuan, Z.; Duan, Z.; Jiang, Y.; Li, X.; Li, Z.; Tai, H. An Ingenious Strategy for Improving Humidity Sensing Properties of Multi-Walled Carbon Nanotubes via Poly-L-Lysine Modification. *Sens. Actuators, B* **2019**, *289*, 182−185.

(43) Wu, J.; Sun, Y. M.; Wu, Z.; Li, X.; Wang, N.; Tao, K.; Wang, G. P. Carbon Nanocoil-Based Fast-Response and Flexible Humidity Sensor for Multifunctional Applications. *ACS Appl. Mater. Interfaces* **2019**, *11*, 4242−4251.

(44) Bulusheva, L. G.; Sysoev, V. I.; Lobiak, E. V.; Fedoseeva, Y. V.; Makarova, A. A.; Dubois, M.; Flahaut, E.; Okotrub, A. V. Chlorinated Holey Double-Walled Carbon Nanotubes for Relative Humidity Sensor. *Carbon* **2019**, *148*, 413−420.

(45) Zhu, C.; Tao, L. Q.; Wang, Y.; Zheng, K.; Yu, J.; Li, X.; Chen, X.; Huang, Y. Graphene Oxide Humidity Sensor with Laser-Induced Graphene Porous Electrodes. *Sens. Actuators, B* **2020**, *325*, No. 128790.

(46) Park, S. Y.; Lee, J. E.; Kim, Y. H.; Kim, J. J.; Shim, Y. S.; Kim, S. Y.; Lee, M. H.; Jang, H. W. Room Temperature Humidity Sensors Based on rGO/MoS2 Hybrid Composites Synthesized by Hydrothermal Method. *Sens. Actuators, B* **2018**, *258*, 775−782.

(47) Davaji, B.; Cho, H. D.; Malakoutian, M.; Lee, J. K.; Panin, G.; Kang, T. W.; Lee, C. H. A Patterned Single Layer Graphene Resistance Temperature Sensor. *Sci. Rep.* **2017**, *7*, 8811.

(48) Li, J.; Chen, X. Y.; Lei, R. B.; Lai, J. F.; Ma, T. M.; Li, Y. Highly Thermally Conductive Graphene Film Produced Using Glucose under Low-Temperature Thermal Annealing. *J. Mater. Sci.* **2019**, *54*, 7553−7562.

(49) Huang, H.; Su, S.; Wu, N.; Wan, H.; Wan, S.; Bi, H.; Sun, L. Graphene-Based Sensors for Human Health Monitoring. *Front. Chem.* **2019**, 399.

(50) Gan, T.; Hu, S. Electrochemical Sensors Based on Graphene Materials. *Microchim. Acta* **2011**, 1−19.

(51) Chen, Z.; Ren, W.; Gao, L.; Liu, B.; Pei, S.; Cheng, H. M. Three-Dimensional Flexible and Conductive Interconnected Graphene Networks Grown by Chemical Vapour Deposition. *Nat. Mater.* **2011**, *10*, 424−428.

(52) Wang, X.; Zhang, Y.; Zhi, C.; Wang, X.; Tang, D.; Xu, Y.; Weng, Q.; Jiang, X.; Mitome, M.; Golberg, D.; Bando, Y. Three-Dimensional Strutted Graphene Grown by Substrate-Free Sugar Blowing for High-Power-Density Supercapacitors. *Nat. Commun.* **2013**, *4*, 1−8.

(53) Miller, J. R.; Outlaw, R. A.; Holloway, B. C. Graphene Double-Layer Capacitor with Ac Line-Filtering Performance. *Science* **2010**, *329*, 1637−1639.

(54) El-Kady, M. F.; Strong, V.; Dubin, S.; Kaner, R. B. Laser Scribing of High-Performance and Flexible Graphene-Based Electrochemical Capacitors. *Science* **2012**, *335*, 1326−1330.

(55) Yang, X.; Cheng, C.; Wang, Y.; Qiu, L.; Li, D. Liquid-Mediated Dense Integration of Graphene Materials for Compact Capacitive Energy Storage. *Science* **2013**, *341*, 534−537.

(56) Pang, Y.; Yang, Z.; Yang, Y.; Ren, T. L. Wearable Electronics Based on 2D Materials for Human Physiological Information Detection. *Small* **2020**, *16*, 1−26.

(57) Lin, J.; Peng, Z.; Liu, Y.; Ruiz-Zepeda, F.; Ye, R.; Samuel, E. L. G.; Yacaman, M. J.; Yakobson, B. I.; Tour, J. M. Laser-Induced Porous Graphene Films from Commercial Polymers. *Nat. Commun.* **2014**, *5*, 1−8.

(58) Ye, R.; James, D. K.; Tour, J. M. Laser-Induced Graphene: From Discovery to Translation. *Adv. Mater.* **2019**, *31*, 1−15.

(59) Rodrigues, J.; Zanoni, J.; Gaspar, G.; Fernandes, A. J. S.; Carvalho, A. F.; Santos, N. F.; Monteiro, T.; Costa, F. M. ZnO Decorated Laser-Induced Graphene Produced by Direct Laser Scribing. *Nano. Adv.* **2019**, 3252−3268.

(60) Zanoni, J.; Moura, J. P.; Santos, N. F.; Carvalho, A. F.; Fernandes, A. J. S.; Monteiro, T.; Costa, F. M.; Pereira, S. O.; Rodrigues, J. Dual Transduction of h2o2 Detection Using Zno/laser-Induced Graphene Composites. *Chemosensors* **2021**, *9*, 102.

(61) Singh, S. P.; Li, Y.; Be'Er, A.; Oren, Y.; Tour, J. M.; Arnusch, C. J. Laser-Induced Graphene Layers and Electrodes Prevents Microbial Fouling and Exerts Antimicrobial Action. *ACS Appl. Mater. Interfaces* **2017**, *9*, 18238−18247.

(62) Ye, R.; James, D. K.; Tour, J. M. Laser-Induced Graphene. *Acc. Chem. Res.* **2018**, *51*, 1609−1620.

(63) Carvalho, A. F.; Fernandes, A. J. S.; Martins, R.; Fortunato, E.; Costa, F. M. Laser-Induced Graphene Piezoresistive Sensors Synthesized Directly on Cork Insoles for Gait Analysis. *Adv. Mater. Technol.* **2020**, *5*, 2000630.

(64) Sajid, M.; Kim, H. B.; Lim, J. H.; Choi, K. H. Liquid-Assisted Exfoliation of 2D hBN Flakes and Their Dispersion in PEO to Fabricate Highly Specific and Stable Linear Humidity Sensors. *J. Mater. Chem. C* **2018**, *6*, 1421−1432.

(65) Zeeshan Yousaf, H. M.; Kim, S. W.; Hassan, G.; Karimov, K.; Choi, K. H.; Sajid, M. Highly Sensitive Wide Range Linear Integrated Temperature Compensated Humidity Sensors Fabricated Using Electrohydrodynamic Printing and Electrospray Deposition. *Sens. Actuators, B* **2020**, *308*, No. 127680.

(66) Dong, Y.; Rismiller, S. C.; Lin, J. Molecular Dynamic Simulation of Layered Graphene Clusters Formation from Polyimides under Extreme Conditions. *Carbon* **2016**, *104*, 47−55.

(67) Dallinger, A.; Kindlhofer, P.; Greco, F.; Coclite, A. M. Multiresponsive Soft Actuators Based on a Thermoresponsive Hydrogel and Embedded Laser-Induced Graphene. *ACS Appl. Polym. Mater.* **2021**, *3*, 1809−1818.

(68) Giannazzo, F.; Fisichella, G.; Piazza, A.; Di Franco, S.; Greco, G.; Agnello, S.; Roccaforte, F. Impact of Contact Resistance on the Electrical Properties of MoS2 Transistors at Practical Operating Temperatures. *Beilstein J. Nanotechnol.* **2017**, *8*, 254−263.

(69) Sahatiya, P.; Puttapati, S. K.; Srikanth, V. V. S. S.; Badhulika, S. Graphene-Based Wearable Temperature Sensor and Infrared Photo-detector on a Flexible Polyimide Substrate. *Flex. Print. Electron.* **2016**, *1*, 25006.

(70) Park, S. Y.; Kim, Y. H.; Lee, S. Y.; Sohn, W.; Lee, J. E.; Kim, D. H.; Shim, Y. S.; Kwon, K. C.; Choi, K. S.; Yoo, H. J.; Suh, J. M.; Ko, M.; Lee, J. H.; Lee, M. J.; Kim, S. Y.; Lee, M. H.; Jang, H. W. Highly Selective and Sensitive Chemoresistive Humidity Sensors Based on rGO/MoS2 van Der Waals Composites. *J. Mater. Chem. A* **2018**, *6*, 5016−5024.

(71) Wang, T.; Zhao, G.; Sun, C.; Zhang, L.; Wu, Y.; Hao, X.; Shao, Y. Graphene-Assisted Exfoliation of Molybdenum Disulfide to Fabricate 2D Heterostructure for Enhancing Lithium Storage. *Adv. Mater. Interfaces* **2017**, *4*, 1−8.

(72) Smith, A. D.; Elgammal, K.; Niklaus, F.; Delin, A.; Fischer, A. C.; Vaziri, S.; Forsberg, F.; Råsander, M.; Hugosson, H.; Bergqvist, L.; Schröder, S.; Kataria, S.; Östling, M.; Lemme, M. C. Resistive Graphene Humidity Sensors with Rapid and Direct Electrical Readout. *Nanoscale* **2015**, *7*, 19099−19109.

(73) Graphene, M. Current Scaling and Dirac Fermion Heating in. **2014**, No. November *2013*, 2−6, DOI: 10.1166/jnn.2014.9038.

(74) Li, N.; Chen, X.-D.; Chen, X.-P.; Ding, X.; Zhao, X. Fast-Response MoS2-Based Humidity Sensor Braced by SiO2 Microsphere Layers. *IEEE Electron Device Lett.* **2018**, *39*, 115−118.

(75) Zhao, J.; Li, N.; Yu, H.; Wei, Z.; Liao, M.; Chen, P.; Wang, S.; Shi, D.; Sun, Q.; Zhang, G. Highly Sensitive MoS2 Humidity Sensors Array for Noncontact Sensation. *Adv. Mater.* **2017**, *29*, 1−7.

(76) Late, D. J.; Huang, Y. K.; Liu, B.; Acharya, J.; Shirodkar, S. N.; Luo, J.; Yan, A.; Charles, D.; Waghmare, U. V.; Dravid, V. P.; Rao, C. N. R. Sensing Behavior of Atomically Thin-Layered MoS2 Transistors. *ACS Nano* **2013**, *7*, 4879−4891.

(77) Wang, Y.; Kim, J. C.; Wu, R. J.; Martinez, J.; Song, X.; Yang, J.; Zhao, F.; Mkhoyan, A.; Jeong, H. Y.; Van Der Chhowalla, M. Waals Contacts between Three-Dimensional Metals and Two-Dimensional Semiconductors. *Nature* **2019**, *568*, 70−74.

(78) Javed, M.; Sajid, M.; Yousaf, H. M. Z.; Hassan, G.; Mahmood, H. Facile and Low Cost Temperature Compensated Humidity Sensor and Signal Conditioning System. *IEEE Sens. J.* **2021**, *21*, 14906−14914.

(79) Shaukat, R. A.; Khan, M. U.; Saqib, Q. M.; Chougale, M. Y.; Kim, J.; Bae, J. All Range Highly Linear and Sensitive Humidity Sensor Based on 2D Material TiSi2 for Real-Time Monitoring. *Sens. Actuators, B* **2021**, *345*, No. 130371.

(80) Syuhada, A.; Shamsudin, M. S.; Daud, S.; Krishnan, G.; Harun, S. W.; Aziz, M. S. A. Single-Mode Modified Tapered Fiber Structure Functionalized With GO-PVA Composite Layer for Relative Humidity Sensing. *Photonic Sens.* **2021**, *11*, 314−324.

(81) Guo, J. Y.; Shi, B.; Sun, M. Y.; Zhang, C. C.; Wei, G. Q.; Liu, J. Characterization of an ORMOCER®-Coated FBG Sensor for Relative Humidity Sensing. *Measurement* **2021**, *171*, No. 108851.

(82) Zhang, J.; Shen, X.; Qian, M.; Xiang, Z.; Hu, X. An Optical Fiber Sensor Based on Polyimide Coated Fiber Bragg Grating for Measurement of Relative Humidity. *Opt. Fiber Technol.* **2021**, *61*, No. 102406.